Tuning the electronic and the crystalline structure of LaBi by pressure: From extreme magnetoresistance to superconductivity

F. F. Tafti,[1,2,*] M. S. Torikachvili,[3] R. L. Stillwell,[4] B. Baer,[4] E. Stavrou,[4] S. T. Weir,[4] Y. K. Vohra,[5] H.-Y. Yang,[1] E. F. McDonnell,[1] S. K. Kushwaha,[2] Q. D. Gibson,[2] R. J. Cava,[2] and J. R. Jeffries[4]

[1]*Department of Physics, Boston College, Boston, Massachusetts, 02467 USA*
[2]*Department of Chemistry, Princeton University, New Jersey, 08540 USA*
[3]*Department of Physics, San Diego State University, San Diego, California, 92182 USA*
[4]*Lawrence Livermore National Laboratory, Livermore, California, 94550 USA*
[5]*Department of Physics, University of Alabama at Birmingham, Birmingham, Alabama, 35294 USA*

(Received 8 July 2016; revised manuscript received 5 December 2016; published 10 January 2017)

Extreme magnetoresistance (XMR) in topological semimetals is a recent discovery which attracts attention due to its robust appearance in a growing number of materials. To search for a relation between XMR and superconductivity, we study the effect of pressure on LaBi. By increasing pressure, we observe the disappearance of XMR followed by the appearance of superconductivity at $P \approx 3.5$ GPa. We find a region of coexistence between superconductivity and XMR in LaBi in contrast to other superconducting XMR materials. The suppression of XMR is correlated with increasing zero-field resistance instead of decreasing in-field resistance. At higher pressures, $P \approx 11$ GPa, we find a structural transition from the face-centered cubic lattice to a primitive tetragonal lattice, in agreement with theoretical predictions. The relationship between extreme magnetoresistance, superconductivity, and structural transition in LaBi is discussed.

DOI: 10.1103/PhysRevB.95.014507

I. INTRODUCTION

Extreme magnetoresistance (XMR) is an enormous increase of electrical resistance in response to a modest magnetic field observed in several topological semimetals including Cd_3As_2, Na_3Bi, NbAs, NbP, TaAs, $NbSb_2$, $TaSb_2$, WTe_2, (Zr/Hf)Te_5 [1–10]. Recent studies on (W/Mo)Te_2 and (Zr/Hf)Te_5 suggest that pressure suppresses the extreme magnetoresistance (XMR) and gives rise to superconductivity [11–14]. Several of these materials show a rapid onset of superconductivity at the pressure where XMR is suppressed, followed by a slow suppression of T_c with further increasing pressure. For example, $MoTe_2$ is superconducting at zero pressure with $T_c = 0.1$ K which rapidly increases to 8 K by applying only 1 GPa of pressure [15]. WTe_2 is not superconducting at $P = 0$, it shows an incomplete superconducting transition at $P = 2.5$ GPa and a full transition at $P = 8$ GPa [11,12]. Similarly, $ZrTe_5$ is not superconducting at $P = 0$, it shows a sudden onset of superconductivity at $P = 6.7$ GPa with a subsequent T_c discontinuity at $P = 20$ GPa attributed to a second superconducting state [13]. By pressurizing LaBi we searched for the above-mentioned characteristics including XMR suppression, superconducting transition, and discontinuous T_c evolution.

The recent interest in LaBi is due to the observation of XMR in this material despite its simple electronic and crystalline structure [16–22]. The three panels of Fig. 1 summarize our main findings:

(a) The suppression of XMR by pressure is a purely electronic effect with no drastic changes in the structural parameters below 5 GPa.

(b) Pressure induces a structural transition at 11 GPa in LaBi.

(c) Superconductivity appears under pressure in LaBi, similar to WTe_2 and $ZrTe_5$.

II. METHODS

Single crystals of LaBi were grown using indium flux and characterized by using powder x-ray diffraction and energy dispersive x-ray spectroscopy as explained in previous works [17,23]. Low-pressure measurements ($P < 2.5$ GPa) were performed in a piston-cylinder clamp cell using 40 : 60 mixture of light mineral oil : n-pentane as a hydrostatic medium. Pressure was measured from the superconducting transition of a Pb gauge placed beside the sample in the clamp cell [24]. The pressure cell was fit to a Quantum Design physical property measurement system (PPMS) which monitored simultaneously the resistance of the sample, the Pb gauge, and a calibrated Cernox sensor attached to the body of the cell for accurate thermometry. High-pressure measurements were performed in a designer diamond anvil cell using steatite as the pressure-transmitting medium and MP35N as the gasket material [25]. The designer diamond had eight tungsten microcontacts centered on a 300 μm culet for electrical transport measurements. Pressure was measured by fluorescent spectroscopy on two pieces of ruby placed beside the sample in the diamond anvil cell [26]. Changes of pressure between room temperature and 10 K are less than 5% based on a low-temperature calibration of rubies with optical fibers. A small single crystal of LaBi ($50 \times 50 \times 10$ μm) was placed inside the 120-μm-diameter sample hole made by the electric discharge method. The two single crystals measured in the clamp cell and the diamond anvil cell come from the same batch. The resistivity and the Hall effect are measured by using the six-probe technique in both positive- and negative-field directions. The data are symmetrized for magnetoresistance and antisymmetrized for the Hall effect.

*fazel.tafti@bc.edu

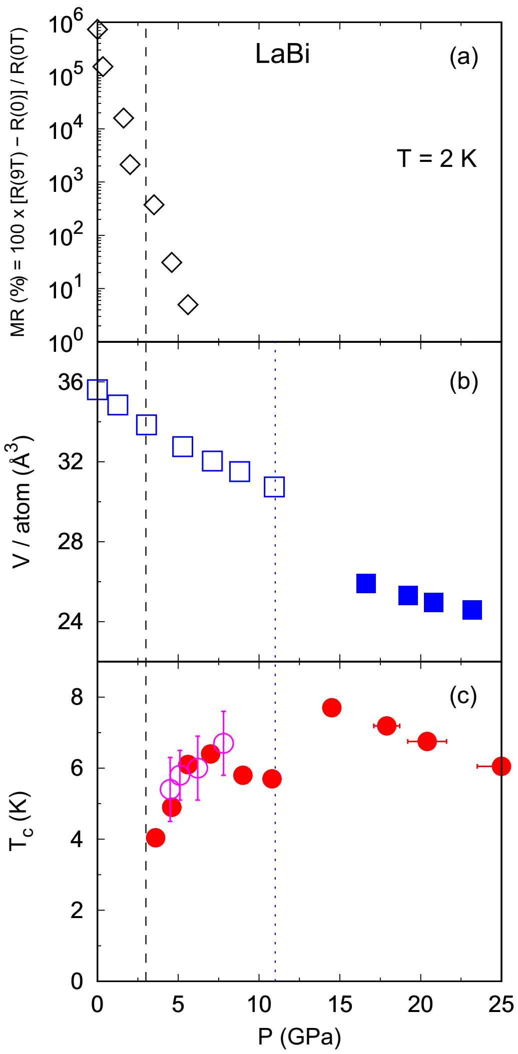

FIG. 1. (a) Magnetoresistance as a function of pressure in LaBi. The extreme magnetoresistance (XMR) is suppressed by $P \approx 5$ GPa. (b) Unit-cell volume per atom as a function of pressure. Pressure reduces the cubic unit-cell volume smoothly across the region of XMR suppression. The discontinuous jump at $P \approx 11$ GPa is a structural transition from cubic to tetragonal marked by the vertical blue dotted line. (c) Temperature-pressure phase diagram of superconductivity in LaBi. The onset of superconductivity is marked by the vertical black dashed line. T_c increases with increasing pressure until $P = 6$ GPa, then decreases until $P = 11$ GPa where it shows a sudden increase concurrent with the structural transition. The red circles show T_c values from resistivity and the open magenta circles show the values from magnetization.

Magnetic measurements of the superconducting transition in LaBi were performed by using a nonmagnetic diamond anvil cell (DAC) inside a commercial superconducting quantum interference device (SQUID) magnetometer. The magnetic background from the cell was accounted for and subtracted carefully, as described in Appendix C. High-pressure x-ray diffraction was performed in a membrane-driven DAC with 300 μm culet diamond anvils and a rhenium gasket with a 120 μm hole filled with LaBi powder, copper powder as the pressure marker, and neon as the hydrostatic medium. Diffraction experiments took place at the Advanced Photon Source at Argonne National Laboratory (beam lines 16 ID-B and 13 ID-D) with 29.2 and 37.1 keV monochromatic x-ray beams. Angle dispersive diffraction patterns were collected with an area detector (Pilatus1M or Mar345) with exposure times ranging from 20 to 120 seconds. Two-dimensional x-ray diffraction images were integrated using FIT2D [27] software and refined using the EXPGUI/GSAS [28] software to extract structural parameters. Band-structure calculations are performed with the WIEN2K program using the general gradient approximation on augmented plane waves and local orbitals [29].

III. RESULTS

Figure 1 summarizes our main findings and provides a guide for the rest of the article. Figure 1(a) shows the suppression of magnetoresistance $\mathrm{MR} = 100\frac{R(9T)-R(0)}{R(0)}$ by pressure. At high pressures, MR reduces to less than a few percent. Figure 1(b) shows smooth compression of the cubic unit cell with no structural anomaly as the extreme magnetoresistance (XMR) is suppressed by pressure. Therefore, the suppression of XMR is due to smooth changes in the electronic structure of LaBi. At $P \approx 11$ GPa a discontinuity occurs in the unit-cell volume due to a structural transition. Figure 1(c) shows that superconductivity ($R = 0$) starts at $P \approx 3.5$ GPa where XMR is substantially but not completely suppressed.

The magenta open circles in Fig. 1(c) are T_c values from magnetic susceptibility measurements, proving bulk superconductivity in LaBi. The susceptibility data are shown in Appendix C. In the rest of the paper, we discuss the effect of pressure on magnetoresistance, crystal structure, and superconductivity in LaBi.

A. The effect of pressure on extreme magnetoresistance

This section presents our data at lower pressures ($P < 2.5$ GPa), from clamp cell experiments, to focus on the suppression of XMR with pressure. Figures 2(a)–2(d) compare the normalized resistance $R(T)/R(300\text{ K})$, at $H = 0$ (blue) and $H = 9$ T (red), at $P = 0$, 0.3, 1.6, and 2.4 GPa. The red curve in Fig. 2(a) shows the typical profile of XMR with $\partial R/\partial T > 0$ at $T > 70$ K, $\partial R/\partial T < 0$ at 20 K $< T <$ 70 K, and $\partial R/\partial T \to 0$ at $T < 20$ K. All topological semimetals with XMR show the same profile where $R(T)$ decreases initially with decreasing temperature, then increases, and finally saturates to a plateau [17]. The blue curve at $H = 0$ shows metallic conduction where $R(T)$ decreases with decreasing temperature to a very small residual value $R(0)$. Such small $R(0)$ is essential to having an extremely large ratio $R(H)/R(0)$, i.e., XMR.

Figures 2(a)–2(d) show a moderate increase of $R(H = 9\text{ T})$ in the *plateau* region ($T < 20$ K) from 0 to 0.3 GPa followed by a decrease at 1.6 GPa and a pronounced decrease at 2.4 GPa. These changes do not account for the systematic suppression of XMR as a function of pressure shown in Fig. 1(a). To understand the systematic decrease of XMR we turn attention to the zero-field resistance $R(H = 0)$. Figures 2(e)–2(h) zoom into the normalized resistance at $H = 0$ and $T < 30$ K at $P = 0$, 0.3, 1.6, and 2.4 GPa to reveal a systematic increase of the zero-field resistance by increasing pressure. The black

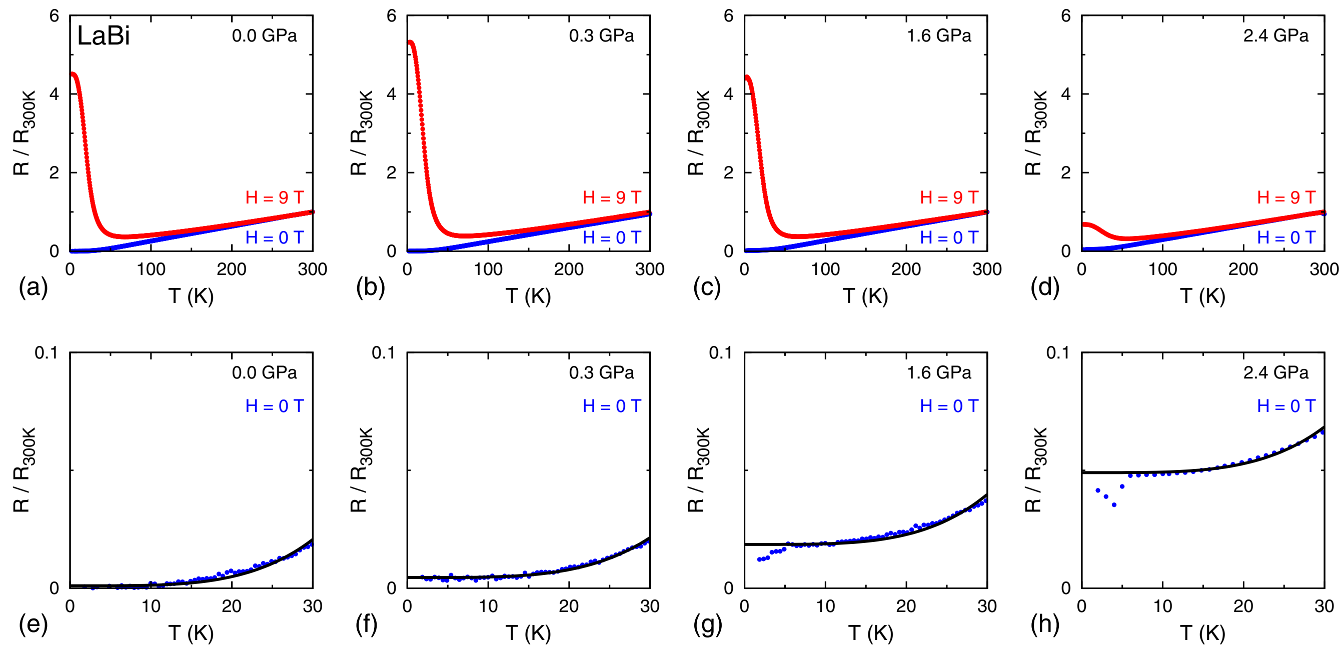

FIG. 2. Normalized resistance $R/R(300\text{ K})$ at $H = 0$ (blue) and $H = 9$ T (red) as a function of temperature at (a) $P = 0$, (b) $P = 0.3$ GPa, (c) $P = 1.6$ GPa, and (d) $P = 2.4$ GPa. The normalized resistance at $H = 9$ T in the plateau region is not systematically suppressed by increasing pressure and therefore does not explain the systematic suppression of XMR with pressure. A zoom into the normalized resistance $R/R(300\text{ K})$ at $H = 0$ is shown for $T < 30$ K at (e) $P = 0$, (f) $P = 0.3$ GPa, (g) $P = 1.6$ GPa, and (h) $P = 2.4$ GPa. Solid black lines are power law fits to extract residual resistances. Broad and incomplete superconducting transitions appear at $P = 1.6$ and 2.4 GPa, most likely due to pressure inhomogeneity.

lines are fits to the expression $R = R_0 + AT^4$ at each pressure. There is no physical meaning to the T^4 function. It simply fits the best to the plateau region of $R(T)$ and estimates R_0 more accurately. The systematic increase of the zero-field resistance in Figs. 2(e)–2(h) explains the systematic decrease of XMR as a function of pressure in Fig. 1(a).

Figure 3(a) visualizes the suppression of XMR with pressure by plotting $\text{MR} = 100\frac{R(H)-R(0)}{R(0)}$ at $T = 2$ K as a function of field at $P = 0$, 0.3, 1.6, and 2.4 GPa. Figure 3(b) shows a clear anticorrelation between increasing $R(0)$ and decreasing magnetoresistance. Both the left and the right y axes are in a logarithmic scale to compare the two quantities on equal footing. In contrast, Fig. 3(c) shows the absence of a clear correlation between $R(9\text{ T})$ and XMR. Comparing Figs. 3(b) and 3(c) makes a compelling case that the zero-field resistance controls the magnitude of XMR in agreement with previous works that correlate the residual resistivity of various LaBi, LaSb, or WTe_2 samples with the magnitude of XMR [9,17,18]. Pressure inhomogeneity, evidenced by broad incomplete superconducting transitions below 2.5 GPa, could lead to additional scattering which increases the residual resistivity and decreases XMR.

B. The effect of pressure on the structure

Figure 4(a) shows that the unit-cell volume of LaBi smoothly decreases with increasing pressure until $P \approx 11$ GPa. There is no structural anomaly at lower pressures where extreme magnetoresistance is suppressed. At 11 GPa there is a discontinuous 10% drop in the unit-cell volume due to a structural transition from the face-centered cubic lattice (fcc, space group $Fm\bar{3}m$) to a primitive tetragonal lattice (PT, space group $P4/mmm$). This is consistent with prior theoretical predictions [30–32] and experimental reports [33]. Figure 4(a) shows that the onset of the structural transition at $P \approx 11$ GPa observed experimentally agrees with the theoretical predictions (thick green lines). Solid black lines in Fig. 4(a) show the Birch–Murnaghan equation of state [34,35]:

$$P(V) = \frac{3B}{2}\left[\left(\frac{V_0}{V}\right)^{\frac{7}{3}} - \left(\frac{V_0}{V}\right)^{\frac{5}{3}}\right] \times \left\{1 + \frac{3}{4}(B'-4)\left[\left(\frac{V_0}{V}\right)^{\frac{2}{3}} - 1\right]\right\}, \tag{1}$$

where P_0 and V_0 are the coordinates of the first data points in the fcc and the PT phases. The bulk modulus B and its pressure derivative $B' = \partial B/\partial P$ in the low-pressure and the high-pressure structures are extracted by fitting Eq. (1) to our data (see Table I). In the low-pressure fcc structure, our experimental value for the bulk modulus agrees with the theoretical calculations by Cui *et al.* [32] and Vaitheeswaran *et al.* [30]. In the high-pressure PT structure, the two theory groups disagree. Cui *et al.* predict comparable bulk moduli between the low- and the high-pressure structures. Vaitheeswaran *et al.* predict a twofold increase of the bulk modulus in the high-pressure PT structure. Our data clearly agree with the latter (see Table I). Representative powder x-ray diffraction data under pressure with Rietveld refinements are shown in Appendix A for both fcc and PT phases.

The structural transition at 11 GPa changes the band structure of LaBi as shown in Figs. 4(b) and 4(c). Figure 4(b)

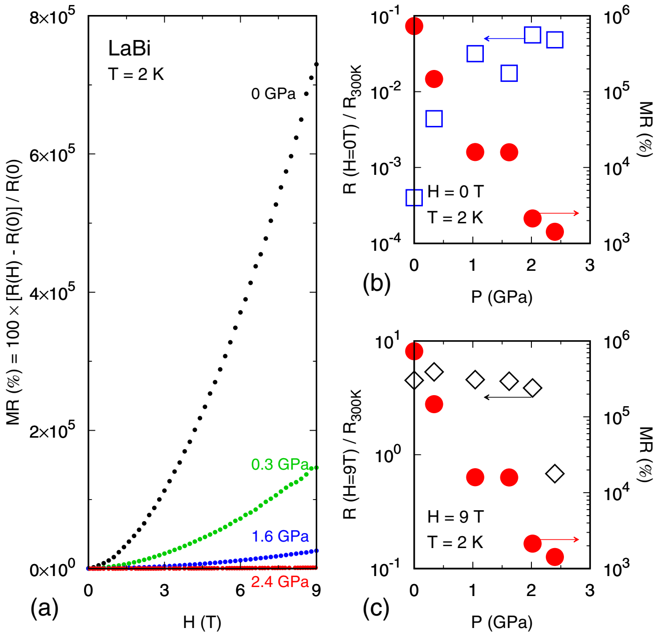

FIG. 3. (a) Magnetoresistance $\mathrm{MR} = 100\frac{R(H)-R(0)}{R(0)}$ at $T = 2$ K plotted as a function of field from $H = 0$ to 9 T at four representative pressure values. A systematic decrease of MR is observed with increasing pressure. (b) Normalized resistance at $H = 0$ and $T = 2$ K are extracted from the fits in Fig. 2 and plotted as a function of pressure (empty blue squares corresponding to the left y axis). MR values at $H = 9$ T and $T = 2$ K are extracted from panel (a) and plotted as a function of pressure (red circles corresponding to the right y axis). Both y axes are logarithmic to show that the two quantities anticorrelate while they vary by orders of magnitude. (c) Normalized resistance at $H = 9$ T and $T = 2$ K are plotted as a function of pressure (empty black diamonds corresponding to the left y axis). MR values at $H = 9$ T and $T = 2$ K are extracted from panel (a) and plotted as a function of pressure (red circles corresponding to the right y axis). There is no clear correlation between the two quantities.

shows the band structure of LaBi in the low-pressure fcc structure with two hole pockets at the Brillouin-zone center Γ and one electron pocket at X. The small circles represent lanthanum d states and the large circles represent bismuth p states. The extremely small $R(0)$ and the large $R(H)$ in LaBi have been attributed to the mixing between d and p states on the electron pocket at X [16,17]. The combination of orbital mixing, small ellipsoidal pockets, and electron-hole compensation as shown in Fig. 4(b) is common to all topological semimetals and is possibly the source of XMR [17].

Figure 4(c) shows the electronic structure of LaBi in the high-pressure PT phase with two notable changes compared with the low-pressure fcc phase: (1) The hole pocket near M is clearly larger than the electron pocket near X and therefore electron-hole compensation is weaker in the PT phase. The lack of electron-hole compensation in the PT phase explains the lack of magnetoresistance at high pressures. (2) There is a band inversion at the R point with a gap due to the spin-orbit coupling. Based on the Fu–Kane–Mele formula [36], this gap corresponds to a strong topological insulator. However, the hole pocket that crosses E_F near M prevents LaBi from being

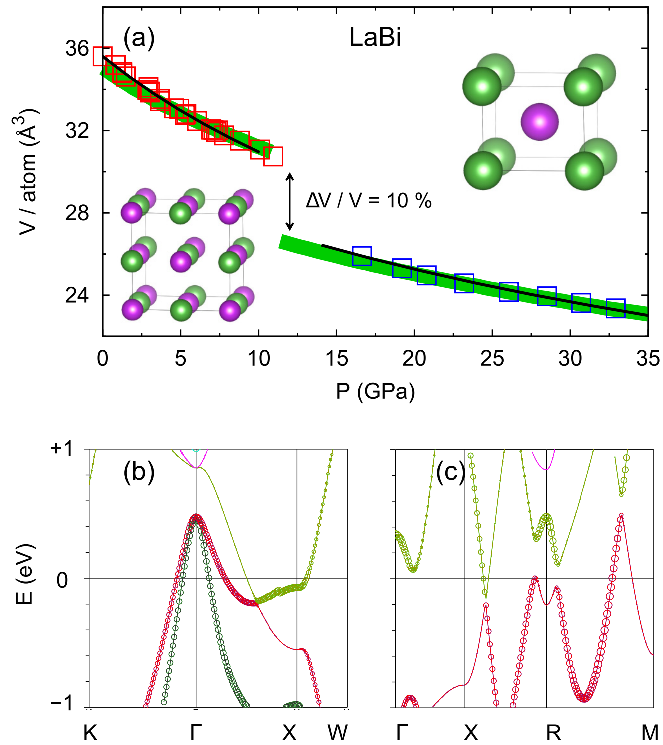

FIG. 4. (a) Unit-cell volume per atom in LaBi as a function of pressure. The discontinuous drop at $P \approx 11$ GPa corresponds to a structural phase transition from face-centered cubic (fcc) to primitive tetragonal (PT) lattice as illustrated on the figure. Thick green lines are the results of theoretical calculations by Vaitheeswaran *et al.* [30]. Solid black lines show the Birch–Murnaghan equation of state [Eq. (1)] from which we extract the bulk moduli for both structures as reported in Table I. Representative refinements are given in Appendix A. (b) Band structure of LaBi in the low-pressure fcc structure with two central hole pockets at Γ and one electron pocket at X. (c) Band structure of LaBi in the high-pressure PT structure with a small electron pocket at X, a larger hole pocket at M, and a gap with band inversion at R.

an insulator. The detailed evolution of the band structure in LaBi under pressure is given in Appendix B.

C. The effect of pressure on superconductivity

Figure 5(a) shows that the first complete superconducting transition ($R = 0$) appears at $P \approx 3.5$ GPa in LaBi. At this pressure, XMR is reduced by three orders of magnitude but has not completely vanished, as shown in Fig. 1(a). Such

TABLE I. The bulk modulus B and its pressure derivative $B' = \partial B/\partial P$ for LaBi extracted from the Birch–Murnaghan equation of state [Eq. (1)] as shown in Fig. 4(a). The initial parameters P_0 and V_0 were fixed based on the experimental data in the low-pressure face-centered cubic (fcc) and the high-pressure primitive tetragonal (PT) structures.

Bravais Lattice	B (GPa)	B'	P_0 (GPa)	V_0 (Å)
fcc	52 ± 1	5.0 ± 0.4	0	35.61
PT	97 ± 5	5.8 ± 0.9	16.6	25.90

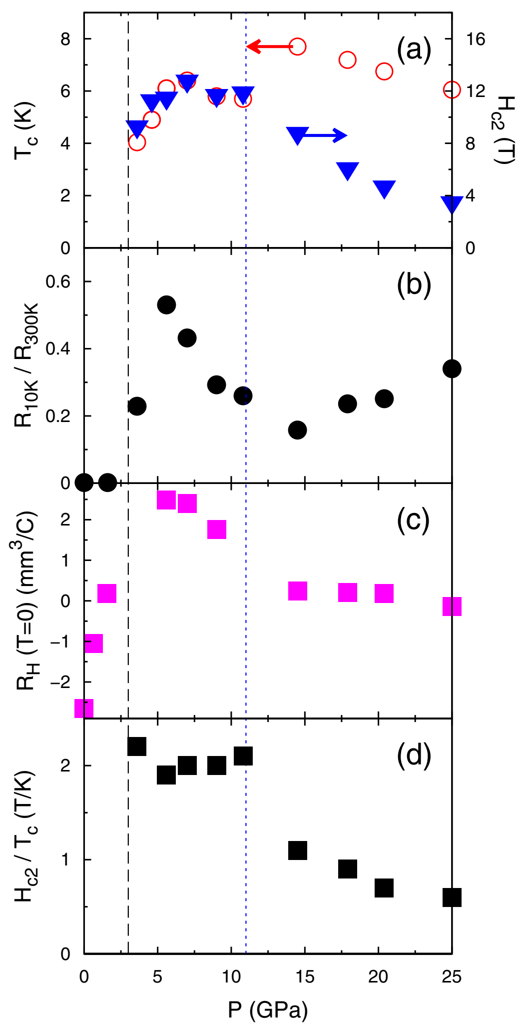

FIG. 5. (a) T_c and H_{c2} of LaBi as a function of pressure. Superconductivity onsets at $P \approx 3.5$ GPa, then T_c shows enhancement at the structural transition at $P \approx 11$ GPa. The onset of superconductivity is shown by a black dashed line and the onset of structural transition is shown by a dotted blue line. (b) R_{10K}/R_{300K} plotted as a function of pressure in LaBi. At the structural transition ($P = 11$ GPa), R_{10K}/R_{300K} reverses direction from decreasing to increasing. (c) The zero-temperature limit of the Hall coefficient R_H as a function of pressure showing a sign change as XMR disappears and superconductivity appears. $R_H \rightarrow 0$ after the structural transition. (d) The ratio H_{c2}/T_c plotted as a function of pressure shows a sudden twofold drop across the structural transition.

coexistence of superconductivity and XMR is absent in WTe_2 and $ZrTe_5$ where superconductivity appears only when XMR completely disappears [11–13].

The onset of superconductivity is accompanied by two other observations, marked by the vertical black dashed line on Fig. 5. First, the normalized low-temperature resistance (R_{10K}/R_{300K}) shows considerable increase at the onset of superconductivity [also see Fig. 5(b)]. Second, the Hall coefficient R_H changes sign [Fig. 5(c)]. The complete temperature profiles of resistivity and Hall data are presented in Figs. 2 and 6. A change of sign in R_H concurrent with superconductivity was recently reported in another XMR material WTe_2

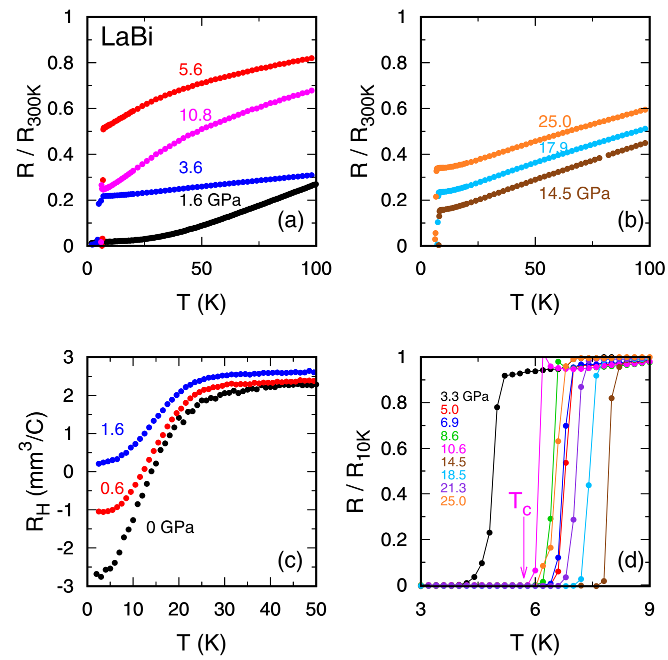

FIG. 6. (a) Normalized electrical resistance at $H = 0$ T, from $T = 2$ to 300 K, at several pressures below 11 GPa before the structural transition. (b) Normalized electrical resistance at $H = 0$ T, from $T = 2$ to 300 K, at several pressures above 11 GPa after the structural transition. (c) Hall coefficient as a function of temperature for several representative pressures. Note the sign change in $R_H(T = 0)$ with increasing pressure. (d) Normalized resistivity curves in the region of superconducting transition from which the phase diagrams in Figs. 1 and 5 are constructed. The arrow on the 10.6 GPa curve shows that we define T_c using $R = 0$ criterion.

[11]. In Appendix B we use the experimental lattice parameters of LaBi to calculate the evolution of its band structure by increasing pressure. Figure 10 in Appendix B shows that the electron pocket size reduces with pressure in agreement with the change of sign in R_H from negative to positive with increasing pressure, as shown in Figs. 5(c) and 6(c). Reference [17] argues that the electron pocket plays a central role in XMR which is consistent with our observation of simultaneous suppression of XMR, sign change in R_H, and the appearance of superconductivity.

The vertical blue dotted line on Fig. 5 marks the onset of structural transition at $P = 11$ GPa as discussed in Sec. III B. After the structural transition, T_c shows a sudden increase [Fig. 5(a)], R_{10K}/R_{300K} reverses direction from decreasing to increasing [Fig. 5(b)], and R_H drops to almost zero [Fig. 5(c)]. The complete $R(T)$ profiles are presented in Figs. 6(a) and 6(b). Such drastic changes in transport properties follow the drastic change of band structure as a result of the structural transition shown in Fig. 4.

Figure 5(a) shows both T_c (left y axis) and H_{c2} (right y axis) at each pressure. Figure 7 shows how we extract H_{c2} of LaBi by using the extended Ginzburg–Landau formalism [37,38]

$$H_{c2}(T) = H_{c2}(0)\frac{1-(T/T_c)^2}{1+(T/T_c)^2}, \quad (2)$$

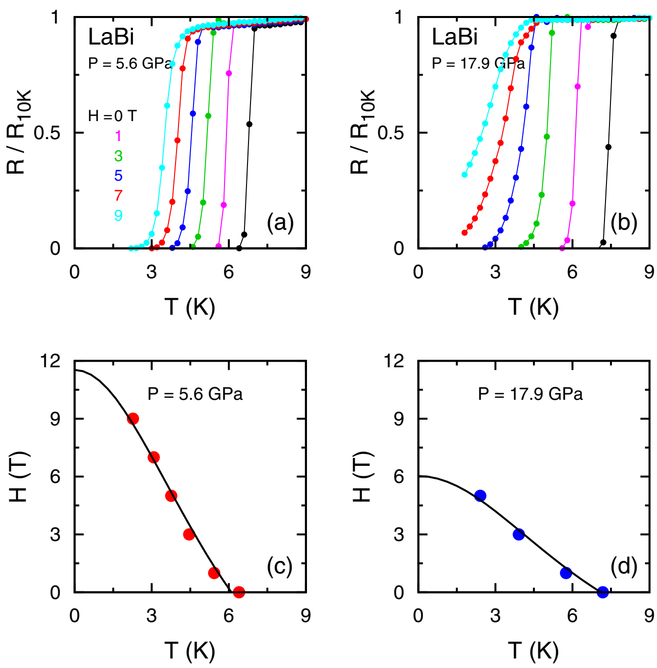

FIG. 7. (a) Normalized electrical resistance at $P = 5.6$ GPa plotted as a function of temperature in several magnetic fields as indicated on the figure. (b) Normalized electrical resistance at $P = 17.9$ GPa plotted as a function of temperature in several magnetic fields. (c) $H_{c2} = 11.5$ T is extracted by fitting Eq. (2) to the H-T data at $P = 5.6$. (d) $H_{c2} = 6.1$ T is extracted by fitting Eq. (2) to the H-T data at $P = 17.9$.

where $H_{c2}(0)$ is the upper critical field at $T = 0$. From Fig. 7, the values of $H_{c2} = 11.5$ T at $P = 5.6$ GPa and $H_{c2} = 6.1$ T at $P = 17.9$ GPa.

Since LaBi is made of two superconducting elements, it is possible that the observed superconducting transitions arise from either La or Bi impurity phases. We compare the T_c-P phase diagrams of La and Bi, with LaBi in Fig. 8. La impurities are unlikely to be the cause of superconductivity, because La has T_c values 4 to 6 K above LaBi at all pressures [39,40]. La metal also superconducts at zero pressure, which is not observed here. Bismuth has T_c values much closer to LaBi especially above 11 GPa, and therefore, filamentary superconductivity from Bi impurities could be responsible for the signature of superconductivity seen at higher pressures ($P > 11$ GPa) [41]. At low pressures ($P < 11$ GPa), however, the two jumps in the T_c of bismuth at 3 and 8 GPa due to structural transitions are absent in our data [42]. The T_c values of LaBi increase continuously from 3.5 to 8 GPa while they decrease in the same pressure range in Bi (Fig. 8). We also observe the superconducting transition in the magnetic susceptibility channel (Appendix C) which is inconsistent with bismuth filamentary superconductivity. The superconducting (SC) volume fraction is estimated to be more than 50%. This qualitative estimate assumes that the powder specimen fills about half the initial sample hole with the demagnetization factor being 0.67 for the ellipsoid geometry. In any case, T_c values of LaBi and Bi are close and, therefore, filamentary superconductivity from Bi impurity is difficult to rule out. The pressure-induced superconductivity in other topological

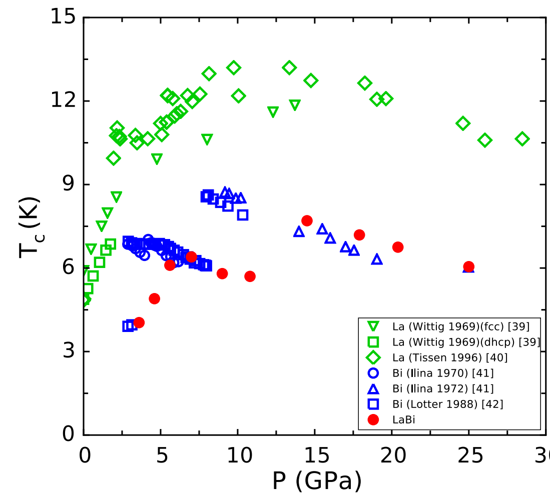

FIG. 8. T_c plotted as a function of pressure in LaBi (red), La (green) and Bi (blue). Data points for La come from Ref. [39]. and [40]. Data points for Bi come from Ref. [41]. and [42]. Superconductivity in La starts from $P = 0$ and shows a dome-like structure with T_c that is 4 to 6 K higher than LaBi at all pressures. Therefore, superconductivity from La impurity is not likely. Superconductivity in Bi starts from $P = 2.5$ GPa with $T_c = 4$ K and shows a profile close to that of LaBi.

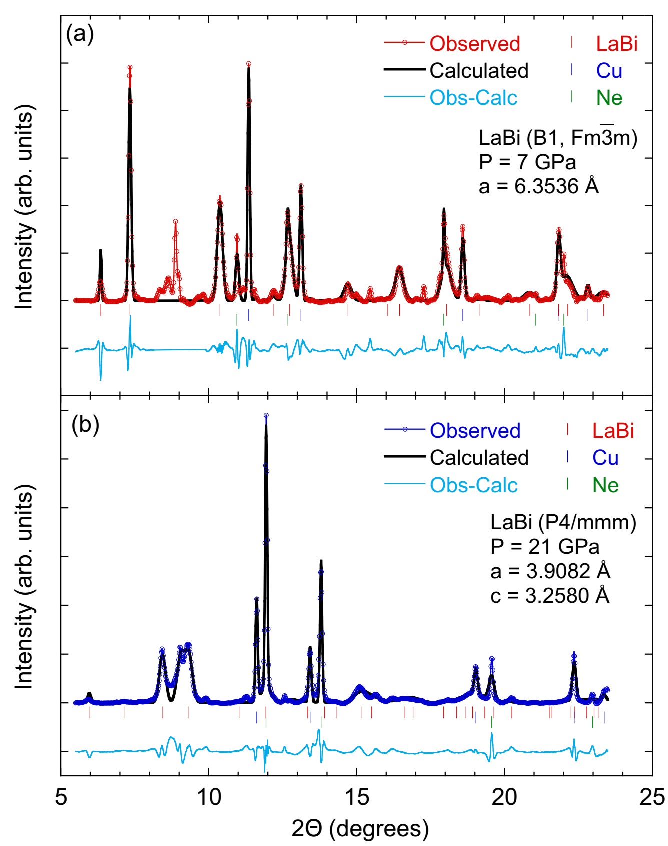

FIG. 9. Representative refinement of the x-ray diffraction patterns collected at (a) $P = 7$ GPa and (b) $P = 21$ GPa. Empty circles show the XRD data plotted as intensity versus 2Θ. Black lines are the best fit to the data. Blue lines show the difference between the data and the fits. Cu (pressure gauge) and Ne (pressure transmitting medium) peaks are indexed individually.

semimetals with XMR have similar issues and more detailed experiments are required to clarify the link between XMR and SC [11–13,15].

Figure 5(a) shows that, before the structural transition at $P = 11$ GPa, H_{c2} values are almost double the value of T_c at each pressure, i.e., $H_{c2}/T_c \approx 2$, but after the transition the H_{c2}/T_c suddenly drops to near unity. Recent studies show a change of T_c with structural transition in $ZrTe_5$ [13]. It would be interesting to look for a similar H_{c2}/T_c drop in $ZrTe_5$ and other XMR materials that superconduct under pressure.

IV. SUMMARY

In summary, we study the effect of pressure on extreme magnetoresistance, crystal structure, and superconducting properties of LaBi. Pressure suppresses XMR and gives rise to superconductivity in LaBi (Fig. 1). The suppression of XMR anticorrelates with the increase of the residual resistance $R(0)$ as shown in Fig. 3(b). It does not correlate with the in-field resistance $R(9\mathrm{T})$ as shown in Fig. 3(c). The suppression of XMR is accompanied by a sign change in the Hall coefficient R_H from negative to positive as shown in Figs. 5(c) and 6(c). Our density functional theory (DFT) calculations in Fig. 10 in Appendix B confirm that the R_H sign change is due to the shrinking of the electron pocket with increasing pressure. The change in the crystal structure changes the band structure and creates a region of band inversion in LaBi (Fig. 4). The changes in the band structure of LaBi due to this structural transition give rise to a reversal in $R_{10\mathrm{K}}/R_{300\mathrm{K}}$ from decreasing to increasing and a drop in R_H as shown in Figs. 5(b) and 5(c). At the structural transition, there is a discontinuity in T_c and in the ratio H_{c2}/T_c (Fig. 5).

ACKNOWLEDGMENTS

We thank Barry Schaudt for installing and running the WIEN2k code on the BC cluster. This work was performed under LDRD (Tracking Code No. 14-ERD-041) and under the auspices of the U.S. Department of Energy (DOE) by Lawrence Livermore National Laboratory (LLNL) under Contract No. DE-AC52- 07NA27344. Portions of this work were performed at HPCAT (Sector 16), Advanced Photon Source (APS), Argonne National Laboratory. HPCAT operations are supported by the DOE-NNSA under Award No. DE-NA0001974 and the DOE-BES under Award No. DE-FG02-99ER45775 with partial instrumentation funding by the NSF. The Advanced Photon Source is a U.S. DOE Office of Science User Facility operated for the DOE Office of Science

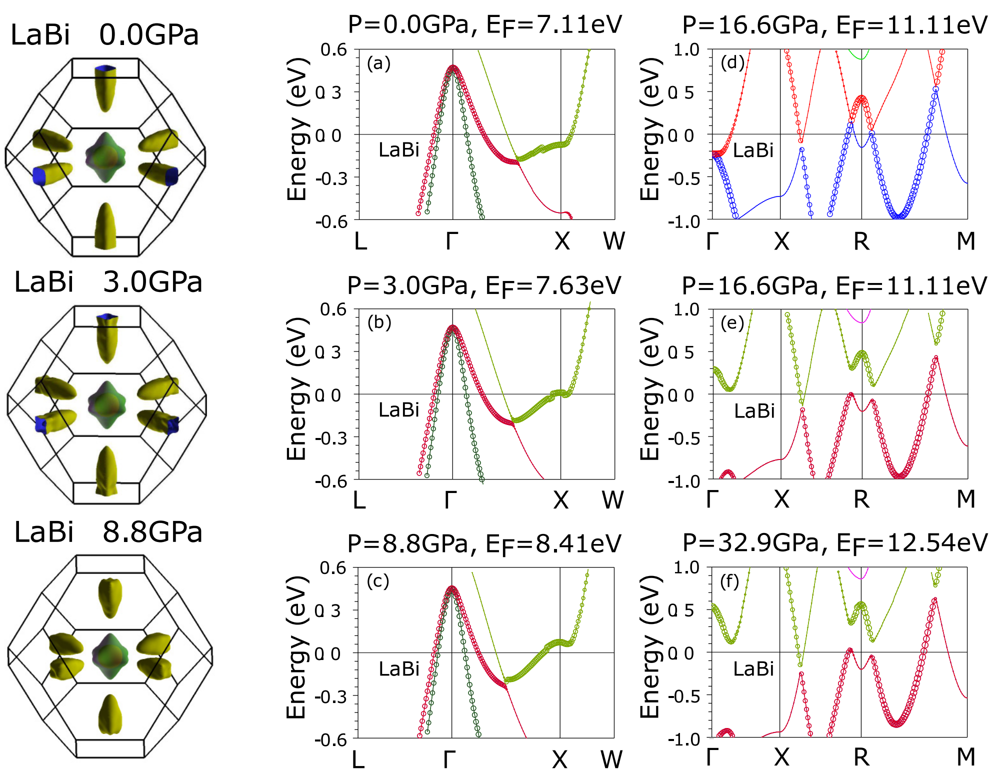

FIG. 10. (a) Band structure of LaBi at $P = 0$ in the fcc structure. The large circles represent the p orbitals of Bi and the small circles represent the d orbitals of La. The y axis is energy relative to E_F with the E_F given on top of each panel. The corresponding Fermi surface is rendered next to the plot. (b) Band structure of LaBi at $P = 3.0$ GPa. Notice that the electron pocket shrinks in size and its shape changes from cylindrical to round. The corresponding Fermi surface is rendered next to the plot. (c) Band structure of LaBi at $P = 8.8$ GPa. The electron pocket continues to shrink and become more spherical. Notice that the Fermi energy E_F increases with increasing pressure and makes the material less compensated. The corresponding Fermi surface is rendered next to the plot. (d) Band structure of LaBi at $P = 16.6$ GPa in the PT structure after the structural transition. This calculation is without spin-orbit coupling to show the mixing between the bands at R. (e) After including SOC, the bands hybridize and a gap opens at R with a clear band inversion. (f) Band structure of LaBi at $P = 32.9$ GPa in the PT structure. Pressure does not change the band structure that much in this phase.

by Argonne National Laboratory under Contract No. DE-AC02-06CH11357. Beam time was provided by the Carnegie DOE-Alliance Center (CDAC). Y.K.V. acknowledges support from DOE-NNSA Grant No. DE-NA0002014. We are grateful to Marcio Siqueira at Almax/EasyLab for use of the magnetic susceptibility diamond anvil cell. The research at Princeton was supported by the Gordon and Betty Moore Foundation under the EPiQS program, grant GBMF 4412 and the ARO MURI on topological insulators, grant W911NF-12-1-0461.

APPENDIX A: RIETVELD REFINEMENT OF HIGH-PRESSURE X-RAY DIFFRACTION DATA

Figure 9 includes two representative structural refinements of the x-ray diffraction data at $P = 7$ GPa and $P = 21$ GPa. The low-pressure structure is rock salt (B_1) and the high-pressure structure has a primitive tetragonal unit cell as illustrated in Fig. 4. In Fig. 9(a), the peaks between 8 and 9 degrees have been excluded from the refinement, and they are likely to come from small inclusions of elemental Bi. At 7 GPa, Bi is in a complex host-guest structure, which is difficult to refine with so few evident peaks. For $P > 8$ GPa, elemental Bi is bcc, and we do include this phase in the refinement; the most prominent Bi peak occurs near 9 degrees in Fig. 9(b).

APPENDIX B: EVOLUTION OF THE BAND STRUCTURE WITH PRESSURE

A recent challenge in condensed-matter physics is to understand the small residual resistance of topological semimetals [43]. In this work, we use pressure to tune the residual resistance of LaBi and study changes to the band structure of the material through DFT calculations. Figures 10(a)–10(c) present the band structure of LaBi in the fcc structure at $P = 0$, 3.0, and 8.8 GPa before the structural transition. Larger circles represent Bi p states and smaller circles represent La d states. The calculation is based on our experimental values for the lattice parameters of LaBi (see Fig. 4). With increasing pressure, the Fermi energy E_F increases which changes both the size and the shape of the electron pocket at X. At high pressures, a large portion of these pockets is teared away, and their shape changes from a cigar shape to a rounded shape. As a result, the quasi-two-dimensional (quasi-2D) structure of these pockets is replaced by a three-dimensional (3D) rounded structure. Figures 10(d)–10(f) present the band structure in the PT structure after the structural transition at $P = 16.6$ and 32.9 GPa. Figure 10(d) shows the results of DFT calculations in the PT structure before including spin-orbit coupling (SOC). As a result of SOC, the two bands that cross at R will hybridize to form a band-inverted gap as shown in Fig. 10(e). Increasing pressure in the PT phase does not change the band structure visibly as shown in Fig. 10(f) which is due to the stiffer structure in the PT phase (Table I). The band structure plotted in Fig. 10(a) gives rise to the extreme magnetoresistance and a negative R_H in LaBi; in Fig. 10(b) XMR is reduced, R_H has changed sign to positive, and the material is on the verge of becoming a superconductor; in Fig. 10(c) XMR is completely gone and the material is superconducting in the fcc structure with $H_{c2}/T_c \approx 2$; in Fig. 10(e) the material has gone through the structural phase transition, it continues to superconduct in the PT structure but with $H_{c2}/T_c \approx 1$; in Fig. 10(f) LaBi is still superconducting in the PT phase with R_H becoming nearly zero.

APPENDIX C: MAGNETIC SUSCEPTIBILITY DATA

Measurements of the superconducting transition in LaBi were performed in a nonmagnetic Almax easyLab Mcell Ultra that fits into the Quantum Design Magnetic Property Measurement System (MPMS). Figure 11 shows superconducting transitions at four different pressures in LaBi from magnetization measurements at $H = 25$ Oe. T_c values are extracted from the peak in $d\chi/dT$ and plotted in Fig. 1(c) as empty magenta circles. The choice of this criterion is based on several test runs with the standard Pb sample. Error bars come from the full width at half maximum (FWHM). The LaBi sample was prepared by grinding a single crystal with a mortar and pestle into a fine powder. The powdered sample was then loaded into the sample chamber along with small (∼15 μm diameter) ruby spheres as a room-temperature pressure marker. No pressure-transmitting medium was used. Pressure was calibrated at room temperature by using the shift in the R1 ruby fluorescence peak with a 5% error to account for the resolution limits of the spectrometer and possible pressure inhomogeneity across the sample. Due to a large magnetic background from the pressure cell compared with the superconducting signal from the sample, we performed a background measurement of the cell, including the empty gasket, at the temperatures and magnetic fields that would be used during the experiment. As a result of a small ferromagnetic signature from the pressure cell there is a small hysteresis that develops with applied fields that needed to be accounted for. After performing several $M(H,T)$ curves, we developed a

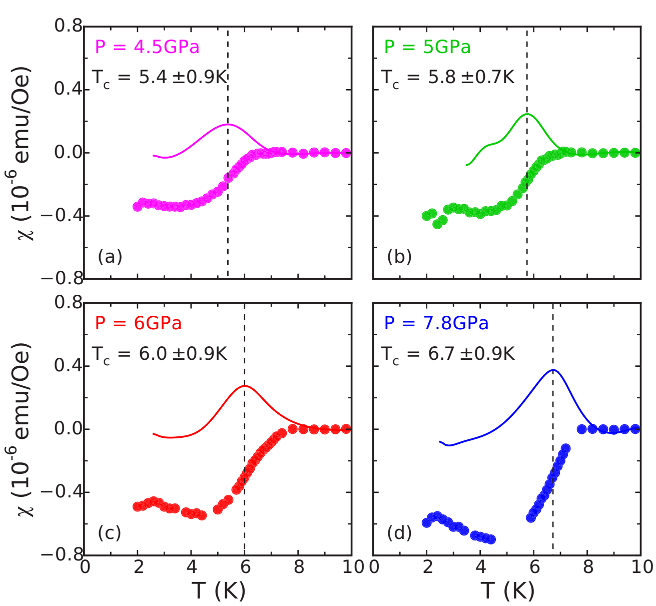

FIG. 11. Superconducting transition from magnetic susceptibility at $P = 4.5$, 5, 6, and 7.8 GPa evidence for the bulk transition in LaBi under pressure. Full circles show data points and solid lines show $d\chi/dT$. T_c is defined as the peak in the derivative curves. The error in T_c is estimated from the FWHM in the peak. Magnetization was measured at $H = 25$ Oe.

procedure of first sweeping the field to 100 Oe, then returning back to 0 Oe at 20 K before beginning zero-field cooling to 2K for our $M(T)$ measurements. This procedure gave the lowest residual and the most reproducible backgrounds. Once a good empty-cell background was acquired at each applied field, the sample was loaded into the pressure cell and the background subtraction algorithm in the MPMS was used in each of the $M(T)$ sweeps to search for T_c in LaBi. The superconducting transition of LaBi was taken as the peak in $d\chi/dT$ vs T.

[1] T. Liang, Q. Gibson, M. N. Ali, M. Liu, R. J. Cava, and N. P. Ong, Nat. Mater. **14**, 280 (2015).
[2] J. Xiong, S. K. Kushwaha, T. Liang, J. W. Krizan, M. Hirschberger, W. Wang, R. J. Cava, and N. P. Ong, Science **350**, 413 (2015).
[3] C. Shekhar, A. K. Nayak, Y. Sun, M. Schmidt, M. Nicklas, I. Leermakers, U. Zeitler, Y. Skourski, J. Wosnitza, Z. Liu, Y. Chen, W. Schnelle, H. Borrmann, Y. Grin, C. Felser, and B. Yan, Nat. Phys. **11**, 645 (2015).
[4] N. J. Ghimire, Y. Luo, M. Neupane, D. J. Williams, E. D. Bauer, and F. Ronning, J. Phys.: Condens. Matter **27**, 152201 (2015).
[5] X. Huang, L. Zhao, Y. Long, P. Wang, D. Chen, Z. Yang, H. Liang, M. Xue, H. Weng, Z. Fang, X. Dai, and G. Chen, Phys. Rev. X **5**, 031023 (2015).
[6] K. Wang, D. Graf, L. Li, L. Wang, and C. Petrovic, Sci. Rep. **4**, 7328 (2014).
[7] Z. Wang, Y. Li, Y. Lu, Z. Shen, F. Sheng, C. Feng, Y. Zheng, and Z. Xu, arXiv:1603.01717.
[8] M. N. Ali, J. Xiong, S. Flynn, J. Tao, Q. D. Gibson, L. M. Schoop, T. Liang, N. Haldolaarachchige, M. Hirschberger, N. P. Ong, and R. J. Cava, Nature (London) **514**, 205 (2014).
[9] M. N. Ali, L. Schoop, J. Xiong, S. Flynn, Q. Gibson, M. Hirschberger, N. P. Ong, and R. J. Cava, Europhys. Lett. **110**, 67002 (2015).
[10] T. M. Tritt, N. D. Lowhorn, R. T. Littleton, A. Pope, C. R. Feger, and J. W. Kolis, Phys. Rev. B **60**, 7816 (1999).
[11] D. Kang, Y. Zhou, W. Yi, C. Yang, J. Guo, Y. Shi, S. Zhang, Z. Wang, C. Zhang, S. Jiang, A. Li, K. Yang, Q. Wu, G. Zhang, L. Sun, and Z. Zhao, Nat. Commun. **6**, 7804 (2015).
[12] X.-C. Pan, X. Chen, H. Liu, Y. Feng, Z. Wei, Y. Zhou, Z. Chi, L. Pi, F. Yen, F. Song, X. Wan, Z. Yang, B. Wang, G. Wang, and Y. Zhang, Nat. Commun. **6**, 7805 (2015).
[13] Y. Zhou, J. Wu, W. Ning, N. Li, Y. Du, X. Chen, R. Zhang, Z. Chi, X. Wang, X. Zhu, P. Lu, C. Ji, X. Wan, Z. Yang, J. Sun, W. Yang, M. Tian, Y. Zhang, and H.-k. Mao, Proc. Natl. Acad. Sci. USA **113**, 2904 (2016).
[14] Y. Qi, W. Shi, P. G. Naumov, N. Kumar, W. Schnelle, O. Barkalov, C. Shekhar, H. Borrmann, C. Felser, B. Yan, and S. A. Medvedev, Phys. Rev. B **94**, 054517 (2016).
[15] Y. Qi, P. G. Naumov, M. N. Ali, C. R. Rajamathi, W. Schnelle, O. Barkalov, M. Hanfland, S.-C. Wu, C. Shekhar, Y. Sun, V. Süß, M. Schmidt, U. Schwarz, E. Pippel, P. Werner, R. Hillebrand, T. Förster, E. Kampert, S. Parkin, R. J. Cava, C. Felser, B. Yan, and S. A. Medvedev, Nat. Commun. **7**, 11038 (2016).
[16] M. Zeng, C. Fang, G. Chang, Y.-A. Chen, T. Hsieh, A. Bansil, H. Lin, and L. Fu, arXiv:1504.03492.
[17] F. F. Tafti, Q. Gibson, S. Kushwaha, J. W. Krizan, N. Haldolaarachchige, and R. J. Cava, Proc. Natl. Acad. Sci. USA **113**, E3475 (2016).
[18] F. F. Tafti, Q. D. Gibson, S. K. Kushwaha, N. Haldolaarachchige, and R. J. Cava, Nat. Phys. **12**, 272 (2016).
[19] L.-K. Zeng, R. Lou, D.-S. Wu, P.-J. Guo, L.-Y. Kong, Y.-G. Zhong, J.-Z. Ma, B.-B. Fu, P. Richard, P. Wang, G. T. Liu, L. Lu, S.-S. Sun, Q. Wang, L. Wang, Y.-G. Shi, H.-C. Lei, K. Liu, S.-C. Wang, T. Qian, J.-L. Luo, and H. Ding, Phys. Rev. Lett. **117**, 127204 (2016).
[20] Y. Wu, T. Kong, L.-L. Wang, D. D. Johnson, D. Mou, L. Huang, B. Schrunk, S. L. Bud'ko, P. C. Canfield, and A. Kaminski, Phys. Rev. B **94**, 081108 (2016).
[21] J. Nayak, S.-C. Wu, N. Kumar, C. Shekhar, S. Singh, J. Fink, E. E. D. Rienks, G. H. Fecher, S. S. P. Parkin, B. Yan, and C. Felser, arXiv:1605.06997.
[22] N. N. Stepanov, N. V. Morozova, A. E. Karâkin, I. V. Korobeinikov, A. V. Golubkov, and V. V. Kaminskii, Phys. Solid State **57**, 1639 (2015).
[23] S. Sun, Q. Wang, P.-J. Guo, K. Liu, and H. Lei, New J. Phys. **18**, 082002 (2016).
[24] A. Eiling and J. S. Schilling, J. Phys. F: Met. Phys. **11**, 623 (1981).
[25] S. T. Weir, J. Akella, C. Aracne-Ruddle, Y. K. Vohra, and S. A. Catledge, Appl. Phys. Lett. **77**, 3400 (2000).
[26] G. J. Piermarini, S. Block, J. D. Barnett, and R. A. Forman, J. Appl. Phys. **46**, 2774 (1975).
[27] A. P. Hammersley, S. O. Svensson, M. Hanfland, A. N. Fitch, and D. Hausermann, High Pressure Res. **14**, 235 (1996).
[28] B. H. Toby, J. Appl. Crystallogr. **34**, 210 (2001).
[29] P. Blaha, K. Schwarz, G. Madsen, D. Kvasnicka, and J. Luitz, *WIEN2K, An Augmented Plane Wave + Local Orbitals Program for Calculating Crystal Properties* (Karlheinz Schwarz, Techn. Universität Wien, Austria, Wien, 2001).
[30] G. Vaitheeswaran, V. Kanchana, and M. Rajagopalan, Phys. B (Amsterdam, Neth.) **315**, 64 (2002).
[31] Z. Charifi, A. H. Reshak, and H. Baaziz, Solid State Commun. **148**, 139 (2008).
[32] S. Cui, W. Feng, H. Hu, Z. Feng, and H. Liu, Solid State Commun. **149**, 996 (2009).
[33] J. Hayashi, T. Toyama, K. Takeda, I. Shirotani, and Y. Ohishi, J. Phys.: Conf. Ser. **215**, 012004 (2010); Photon Factory Activity Report 23 (2006).
[34] F. D. Murnaghan, Am. J. Math. **59**, 235 (1937).
[35] F. Birch, Phys. Rev. **71**, 809 (1947).
[36] L. Fu, C. L. Kane, and E. J. Mele, Phys. Rev. Lett. **98**, 106803 (2007).
[37] X. Zhu, H. Yang, L. Fang, G. Mu, and H.-H. Wen, Supercond. Sci. Technol. **21**, 105001 (2008).
[38] L. Fang, Y. Wang, P. Y. Zou, L. Tang, Z. Xu, H. Chen, C. Dong, L. Shan, and H. H. Wen, Phys. Rev. B **72**, 014534 (2005).

[39] M. B. Maple, J. Wittig, and K. S. Kim, Phys. Rev. Lett. **23**, 1375 (1969).
[40] V. G. Tissen, E. G. Ponyatovskii, M. V. Nefedova, F. Porsch, and W. B. Holzapfel, Phys. Rev. B **53**, 8238 (1996).
[41] M. Il'ina, E. Itskevich, and E. Dizhur, Zh. Eksp. Teor. Fiz. **61**, 2357 (1972) [Sov. Phys. JETP **34**, 1263 (1972)].
[42] N. Lotter and J. Wittig, Europhys. Lett. **6**, 659 (1988).
[43] Q.-D. Jiang, H. Jiang, H. Liu, Q.-F. Sun, and X. C. Xie, Phys. Rev. B **93**, 195165 (2016).